Applied Physics A (2018) 124:457
https://doi.org/10.1007/s00339-018-1874-0

Applied Physics A
Materials Science & Processing

Electron trapping in the photo-induced conductivity decay in GaAs/SnO_2 heterostructure

Cristina de Freitas Bueno[1] · Luis Vicente de Andrade Scalvi[1]

Received: 6 February 2018 / Accepted: 25 May 2018 / Published online: 29 May 2018
© Springer-Verlag GmbH Germany, part of Springer Nature 2018

Abstract
The decay of photo-induced conductivity is measured for GaAs/SnO_2 heterostructure, after illumination with appropriate wavelength. The top oxide layer is deposited by sol–gel-dip-coating and doped with Eu^{3+}, and the GaAs bottom layer is deposited by resistive evaporation. It shows quite unusual behavior since the decay rate gets slower as the temperature is raised. The trapping by intrabandgap defects in the SnO_2 top layer is expected, but a GaAs/SnO_2 interface arrest becomes also evident, mainly for temperatures below 100 K. Concerning the SnO_2 layer, trapping by different defects is possible, due to the observed distinct capture time range. Besides Eu^{3+} centers and oxygen vacancies, this sort of heterostructure also leads to Eu^{3+} agglomerate areas in the SnO_2 top layer surface, which may contribute for electron scattering. The electrical behavior reported here aims to contribute for the understanding of the electrical transport mechanisms which, combined with emission from Eu^{3+} ions from the top layer of the heterostructure, opens new possibilities for optoelectronic devices because samples in the form of films are desirable for circuit integration. The modeling of the photo-induced decay data yields the capture barrier in the range 620–660 meV, and contributes for the defect rules on the electrical properties of this heterostructure.

1 Introduction

When a semiconductor sample is illuminated with light of appropriate wavelength, intrabandgap defects are ionized and, depending on the irradiating light energy, also band-to-band excitation may take place. When the illumination is removed and the decay of the current is monitored, the resulting conductivity may be modeled, yielding information on several relevant kinetics parameters, related to the electron trapping by these defects. The issue treated here is the analysis of this decay, when the wide bandgap oxide semiconductor tin dioxide (SnO_2) is deposited on top of a GaAs layer. Wide bandgap oxide semiconductors have offered growing interest due to its relevance in transparent optoelectronic devices, among other applications [1–3]. SnO_2 may be included in this category because has a wide bandgap of about 3.6–4.0 eV, and above 90% transparency in the visible range [4]. SnO_2 is naturally an n–type semiconductor, due mainly to the non-stoichiometry that originates oxygen vacancies, which in conjunction with Sn interstitial atoms causes this insulating metallic oxide to behave as a semiconductor. This compound can be doped with several types of ions giving rise to modified properties. Doping SnO_2 with Sb^{5+} by the sol–gel process leads to improved n-type conductivity, due to donor character of pentavalent Sb ions, even though the mobility is low, due to rather small grains [5]. Recently Nd-doped SnO_2 thin films deposited by the RF magnetron sputtering at different temperatures [6] have also shown improvement of the n-type character, carrier concentration, resistivity and mobility with deposition temperatures up to 300 °C. Structural and electrical characteristics of the SnO_2 samples were also significantly affected by Pt-doping [7]. The temperature dependence of the electrical conductivity of undoped, and Cu, Al and In-doped SnO_2 deposited on glass substrate by spray pyrolysis [8] has shown an almost constant behavior in the range 120–300 K, and changes gradually in the temperature range of 300–400 K. The electrical conductivity of SnO_2 film decreased with doping with Al^{3+}, In^{3+} and Cu^{2+} in the whole investigated temperature range, that can be explained by the coexistence of donors (intrinsic point defects such as oxygen vacancies and tin interstitials, as already mentioned), and acceptors (substitution of Sn^{4+} by In^{3+}, Cu^{2+} or Al^{3+}) which compensate each other.

✉ Luis Vicente de Andrade Scalvi
scalvi@fc.unesp.br

[1] Department of Physics-FC and POSMAT, Post-graduate program in Materials Science and Technology, UNESP, São Paulo State University, Bauru, SP, Brazil

Rare-earth-doped wide bandgap semiconductors present luminescent emission with high quantum efficiency [9, 10]. Incorporation of trivalent rare-earth ions such as Eu^{3+} in the SnO_2 layer leads to high charge compensation since the doping ions acts as acceptors in the naturally n-type matrix. Another effect of the trivalent rare-earth ion incorporation is the decreasing of the crystallite size, which leads to higher grain boundary electronic scattering [11], decreasing the mobility. The emission of Eu^{3+} has been made possible in this heterostructure, which does not happen for a sole film of Eu-doped SnO_2 [12]. The observed dominant transition depends on the ion location: the $^5D_0 \rightarrow {}^7F_1$ is dominant when the ions are preferentially located at substitutional Sn sites, whereas the $^5D_0 \rightarrow {}^7F_2$ transition turned out as the most intense when most of the ions are located at grain boundary layers [10]. Besides, the thermal annealing temperature of the heterostructure may increase the crystallite size and increase the population of Eu^{3+} in substitutional sites [12].

The bottom layer for the heterostructure GaAs/SnO_2:2at%Eu^{3+} investigated in this paper is gallium arsenide (GaAs), which is a high-mobility semiconductor, and direct bandgap transition, of 1.42 eV, evaluated for single crystal [13].

Combining the individual films as heterojunctions may be an interesting way of improving the device properties. SnO_2 heterostructures have been successfully used such as with gallium selenide (GaSe) [14]. Hierarchical SnO_2 nanostructures (HTNs) prepared by hydrothermal process [15] provided a unique morphology, and fast ion and electron transfer characteristics, showing excellent super capacitor performances. Van der Waals heterostructure device platform, in which an atomically thin MoS_2 layer was encapsulated by hexagonal boron nitride and contacted by graphene [16], provided a standard device platform that enabled measuring the intrinsic electrical transport of two-dimensional materials and achieve high-mobility two-dimensional devices. P–n heterojunction diodes, where thin black phosphorus layers are interfaced with highly n-doped GaAs substrate [17], exhibited a close-to-ideal diode behavior while under illumination they display a photoresponse with high efficiency.

Besides the Eu^{3+} emission that in the heterostructure can be significantly improved [12], previous reports relate that the SnO_2 and GaAs combination in a heterostructure may improve the electrical properties [18–21]. Then, to acquire knowledge on the application of these devices in optoelectronics, this report focuses on investigation of photo-induced electrical properties of this heterostructure.

The photo-induced conductivity decay has its principle related to the phenomenon of persistent photoconductivity (PPC), property associated to defects that exhibit large lattice relaxation [22], and then the metastable photo-induced conductivity state may last a practically infinite time, when the lattice does not have enough thermal energy to relax. PPC has been found in rare-earth-doped SnO_2 [23], besides SnO_2 nanobelts [24] and quantum dots [25]. Modeling the decay of PPC in a single layer of sol–gel-deposited SnO_2, mainly considering the nanosized grains of this material, has led to relevant electron transport parameters, such as energy capture and grain boundary potential barrier [26]. Possibility of PPC in the heterostructure GaAs/SnO_2 has been found recently [20] for room temperature experiments and then, a complete analysis of the decay of PPC, taking the temperature as variable parameter, is reported here. The great novelty of this paper compared to previously reports is that, besides the trapping by material defects, there is the possibility of carrier trapping at the interface potential barrier. Published PL spectra [12] for this sort of heterostructure in combination with the present paper, shows its potentiality to the creation of electroluminescent devices or other sort of optoelectronic devices, such as amplifiers.

2 Experimental approach and basis for data analysis

2.1 Heterostructure thin film deposition

GaAs thin film deposition was described elsewhere [7], and comprises basically the resistive evaporation technique, in a BOC Edwards evaporator system model AUTO 500. The evaporation of GaAs occurs due to the low pressure inside the chamber, allowing a beam of the material in the gaseous phase to be directed to the substrate, attached to a rotating plate, which assures homogeneous composition and thickness of deposited films.

Details on the deposition of Eu-doped SnO_2 thin films have also been published elsewhere [10], being prepared through the sol–gel route, using $SnCl_4.5H_2O$ (0.5 M), and Eu_2O_3 for doping. The Eu^{3+} composition used in this report (2at% in the SnO_2 layer) was determined from a mass calculation in the sol–gel solution preparation. Deposition of Eu^{3+}-doped SnO_2 thin film layer was carried out in air atmosphere (room temperature) on top of GaAs layer, and after each dip-coated layer, samples were dried in air by 20 min and treated at 200 °C by 10 min in the same oven used for GaAs annealing. This procedure was repeated ten times. The heterostructure final annealing temperature was 200 °C by 1 h.

To make the sample assembly clearer, the processing steps are schematized in Fig. 1. The substrate is a soda-lime glass piece, where a GaAs layer is deposited by the resistive evaporation technique. The 2at%Eu^{3+}-doped SnO_2 film is deposited by sol–gel-dip-coating process, and In contacts are deposited on top of it also by resistive evaporation, using a shadow mask, followed by a thermal annealing at 150 °C

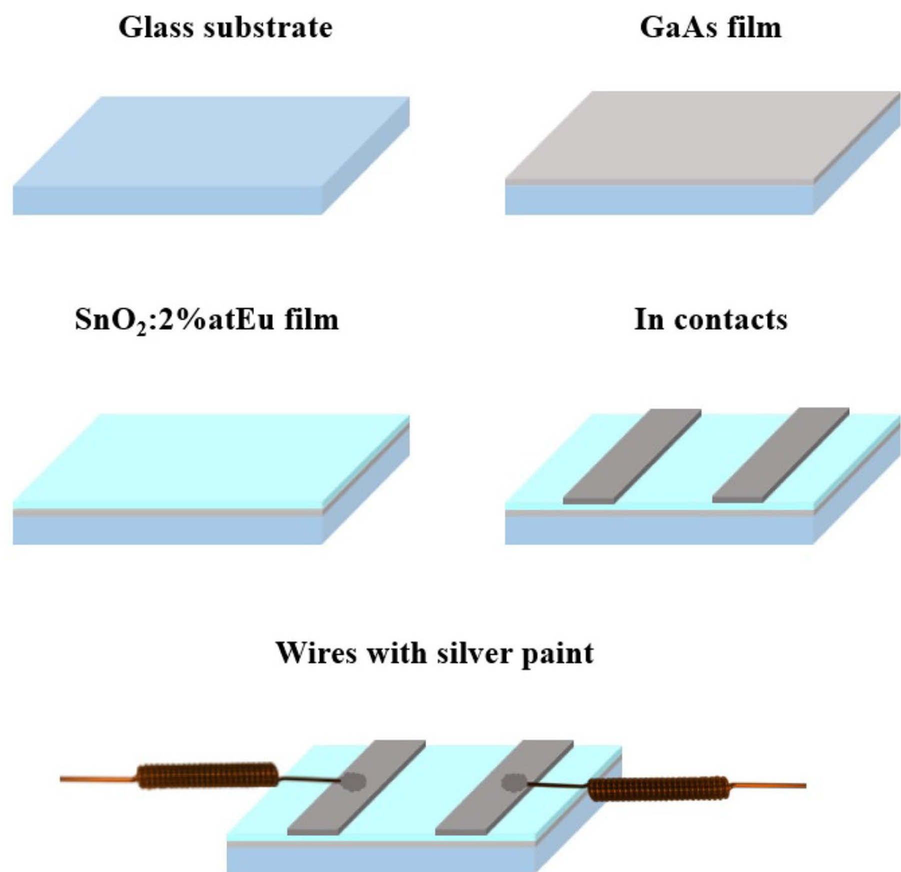

Fig. 1 Diagram of sample processing: a GaAs layer is deposited on glass substrate by resistive evaporation, followed by a 2at%Eu^{3+}-doped SnO_2 film deposited by sol–gel-dip-coating, and resistively evaporated In contacts. Copper wires are attached using silver paint

by 30 min. To provide electrical contacts to the equipment, located outside the cryostat, copper wires are attached on the In contacts using silver paint, which is dried by UV light.

2.2 Microscopy

Surface morphological characterization and a scanning of compositional analysis on the surface were accomplished with scanning electron microscopy (SEM) system of FEI, model Quanta 200, equipped with an energy-dispersive X-ray (EDX) microanalysis system from Oxford, model Inca 250P20. Metallization was carried out with gold (Au) deposition in an Edwards Scancoat Six sputter coater system. Electrons were accelerated under 25 kV for EDX analysis.

2.3 Electrical characterization through decay of photo-induced conductivity

Electrical characterization was carried out using a Keithley electrometer model 6517. The GaAs/SnO_2:2%Eu sample was placed in a Janis He-closed cycle cryostat with a compressor CTI-Cryogenics, coupled to a Lake-Shore temperature controller, which controls the temperature with precision of 0.05 K. For the decay of photo-induced conductivity measurements, the sample was irradiated with InGaN LED (450 nm, 2.76 eV) and He–Cd laser (325 nm, 3.82 eV) in different temperatures (50, 75, 100, 150, 190 and 200 K). These sources were chosen due to the high intensity and monochromatic energy: the InGaN LED has energy above the GaAs bandgap (1.42 eV in the single crystal form), and below the SnO_2 bandgap (about 3.6 eV), whereas the He–Cd laser has energy above the SnO_2 bandgap. Considering that the top layer is SnO_2, the InGaN LED may excite intrabandgap defect states in SnO_2, or band-to-band in GaAs, considering that it may reach the bottom GaAs layer.

The procedure of this experiment consists, basically, of irradiating monochromatic light of appropriate wavelength until current saturation, and measuring the current decay as function of time. The time for saturation was assumed as 9 min of continuous irradiation, keeping constant temperature and the voltage applied by the electrometer was 5 V.

This experiment is very useful to investigate thermally activated defects, mainly when subject to a lattice relaxation [27, 28]. To model this decay, the sample resistance as function of time for a fixed temperature can be seen as the simple relation $R(t) = K_s \cdot [n(t) \cdot \mu(t) \cdot q]^{-1}$, where K_s is a constant (proportionality factor between resistance and resistivity), $n(t)$ is the time-dependent electron concentration, $\mu(t)$ is the time-dependent electronic mobility and q is the electron charge.

The observed decay of conductivity as function of time means that the resistance of the film increases with time. The decay of photo-induced electrons (n) from the conduction band to the trapping defect is given by a simple differential equation [28], whose solution has been previously published [28, 29]. The average crystallite size, evaluated from line broadening of XRD pattern is about 5–8 nm [30]. Then, we may consider that mobility (μ) is dominated by grain boundary scattering, and neglect bulk scattering mechanisms (phonon and ionized impurity). It is important to mention that this situation is different from a recent study by Boyalı and coworkers [31], who concluded that electron–electron scattering is dominating at low temperatures while the electron–phonon scattering is the dominant mechanism at high temperatures. In that case, samples were deposited by magnetron sputtering, which leads to larger grains, and the free electron concentration is associated to a completely degenerate semiconductor. In our case, the mobility due to grain boundary scattering is proportional to $T^{-1/2} \cdot \exp(-\phi \cdot k^{-1}\ T^{-1})$ [32], where ϕ is the grain boundary potential barrier. After substituting terms and a straightforward algebraic simplification, one obtains:

$$R(t) = C_1 + K_2 \cdot T \cdot \exp\left(-\frac{E_{\mathrm{cap}} - \phi}{kT}\right) \cdot t, \tag{1}$$

where C_1 is temperature dependent but not time dependent [26, 29]. E_{cap} is the potential barrier for electron trapping, related to lattice relaxation and ϕ is the grain boundary potential barrier. K_2 is a combination of constant values, including the grain boundary scattering constant, the proportionality factor constant between resistance and resistivity, and the constant capture cross-section (infinite temperature).

Equation (1) demonstrates that $R(t)$ is a linear function of time for fixed temperature. Evaluating the first derivative and calling it as tgR can be easily found that a plot of $\ln(tgR/T)$ as function of $1/T$ yields the quantity $(E_{\mathrm{cap}}-\phi)$ directly from the curve inclination. Taking into account the temperature dependence of the capture cross-section ($\gamma_n \propto \exp(-E_{\mathrm{cap}}/kT)$), it is expected that a capture rate increases with the temperature increase, as reported for other thermally activated defects [28, 29, 33]. It is important to state that the modeling proposed to quantify the decay takes into account only the photo-ionization of defects in the top SnO_2 layer. In the case of this paper, there is another possibility, since the assembly in a heterostructure leads to the possibility of electron transfer between layers and then the time-dependent conductivity may be affected. Then, the modeling is applied to the observed experimental photo-induced conductivity decay data, and possible deviations from the expected behavior are qualitatively explained considering the bottom GaAs layer influence.

3 Results and discussion

3.1 Photo-induced current decay data and model

Figure 2 shows the current decay for the heterostructure sample GaAs/SnO_2:2%Eu. The excitation was accomplished using two monochromatic light sources: Fig. 2a: InGaN LED (450 nm, 2.76 eV), and Fig. 2b: He–Cd laser (325 nm, 3.82 eV). In both cases, the current increase was obtained by sample irradiation until the saturation, which is practically obtained with 9 min of excitation. In Fig. 2b, the decay at 75 K is not shown because it does not follow the general tendency, presenting oscillations at time zero and a much sharper decay, that crosses the other curves, which is probably related to contact instability, since the In metallic contact was loosen from the sample just after taking this data set. Considering that the evaporation of new In contacts, followed by connecting copper wires with silver paint

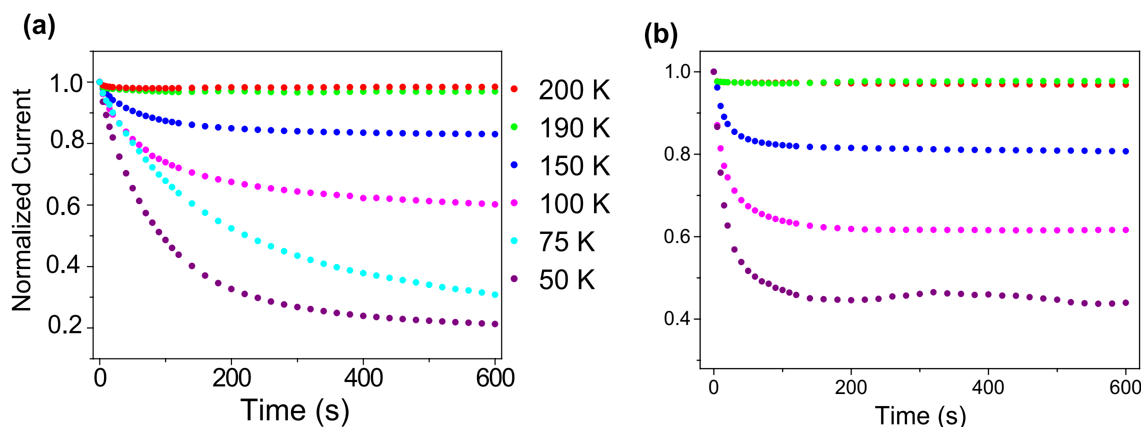

Fig. 2 Photo-induced current decay for heterostructure GaAs/SnO_2:2%Eu treated at 200°C/1 h, excited with two distinct monochromatic light sources: **a** LED InGaN (450 nm) and **b** laser He–Cd (325 nm)

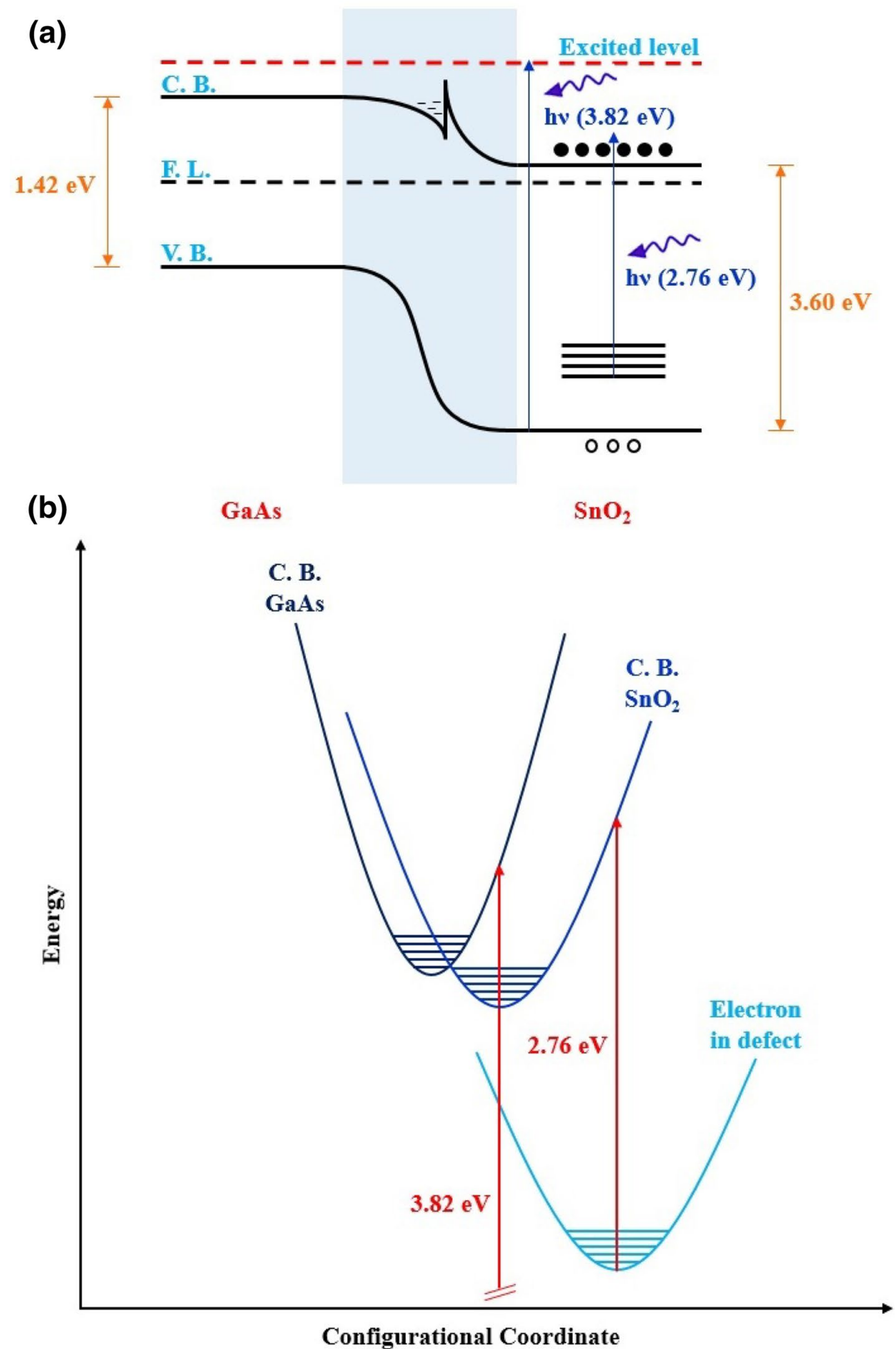

Fig. 3 (Top) Heterostructure band diagram showing the two sorts of excitation: He–Cd laser (3.82 eV) and InGaN LED (2.76 eV). (Bottom) Configurational coordinate diagram showing the electronic vibration at an average defect level and at conduction band of SnO_2 and GaAs. Vertical red lines indicate the optical excitation from defects and from valence band of SnO_2

could affect the sample original characteristics (SnO_2 is a well-known gas sensor), it was not possible to reproduce the decay at 75 K with laser excitation. Anyway, it does not spoil the interpretation since all the other data sets were quite consistent, allowing the process quantification.

Figure 2 allows observing that, after removal of the excitation source in both cases (LED or laser irradiation), the decay magnitude is temperature dependent, becoming slower as the temperature is increased, which is a surprising result, since the trapping by defects is a thermally activated process, and the decay should be slower for lower temperature as observed previously for other semiconductors such as Si-doped AlGaAs or Er and Eu-doped SnO_2 [28, 29, 33]. However, this sort of decay, seen in Fig. 2, has been observed before for Sb-doped SnO_2 [34]. Comparing Fig. 2a, b, it is clearly observed that the decay shows a strong dependence

Table 1 Values of electrical current for the decay measurements at different temperatures for the heterostructure GaAs/SnO_2:2%Eu

GaAs/SnO_2:2%Eu	Excitation LED InGaN ($\lambda = 450$ nm)			Excitation laser He–Cd ($\lambda = 325$ nm)		
Temperature (K)	I_{dark} (nA)	$I_{initdecay}$ (nA)	I_{after} (nA)	I_{dark} (nA)	$I_{initdecay}$ (nA)	I_{after} (nA)
50	2.207	13.610	2.891	0.610	1.503	0.661
75	15.658	63.085	19.436	–	–	–
100	29.842	50.904	30.637	25.9	43.8	27.0
150	189.57	230.72	191.59	189.9	238.3	192.4
190	634.0	655.3	635.2	768.8	812.1	793.9
200	818.4	833.8	820.5	1026.8	1093.3	1059.2

I_{dark} current before excitation with light source, $I_{initdecay}$ maximum current (saturation) due to excitation during 9 min, I_{after} current after decay measurement (10 min)

with light source. Laser excitation leads, in general, to a slower decay when compared to excitation with the LED. Considering that the laser has above SnO_2 bandgap light, it is expected that more carriers are excited, including electron–hole pair generation, whose recombination is supposed to yield a faster decay. However, the slower decay suggests that electrons may be excited to overcome the potential barrier at the interface GaAs/SnO_2, becoming located at the GaAs side, and keeping the sample in a high conductive state, which slowly returns to the equilibrium state. Figure 3 sketches this possibility. On the other hand, the relatively faster decay in the case of InGaN LED excitation means that the only intrabandgap defects are excited and electrons are raised to a lower energy state, remaining in the SnO_2 side of the heterostructure. The excitation by the LED (energy of 2.76 eV) is also in good agreement with the PL data [12] which shows a broad band as originated from a transition between acceptors and donors. In this case, the Eu^{3+} acts as acceptors, which explains why this energy does not excite electrons to overcome the interface potential barrier, since acceptors are located deeper in the bandgap, closer to the valence band. Figure 3 is a sketch of the configurational diagram, including the vibrational states in the conduction bands of the two materials and in the symbolic deep level, probably Eu^{3+} acceptor level. In this diagram, the crossing between the GaAs and SnO_2 parabolas represents the interface energy barrier between electrons belonging to these conduction states. The optical excitation is represented by vertical lines.

Concerning the current excitation, although the grain boundary mobility decreases with temperature increase, the effect of ionizing more defects with light irradiation at higher temperatures compensates the mobility influence, besides the equilibrium statistical electron density leads to more ionization to higher temperatures. The overall result is a higher conductivity for higher temperature (not shown in Fig. 2, since the plotted current is normalized, but can be seen in Table 1). On the other hand, the slower decay with increasing temperature is related with the time and temperature dependency of the nanoparticle boundary layer barrier height concomitant with boundary layer depletion layer width. The increase in the barrier height with temperature is similar to reported data for Sb-doped SnO_2 [34]: the temperature influence on the decay may be associated with the growth of the barrier height and depletion layer between grains. A similar effect may be used to explain the time dependence: Eu^{3+} acceptor ions are located preferentially at substitutional sites close to the grain boundary layer, surrounded by oxygen vacancies [30], which are trapping defects. As time passes, the trapping increases the barrier height besides the depletion layer width, being more efficient at higher temperatures by the thermal influence in the grain boundary mobility [34]. Therefore, with the temperature increase, the mobility influence seems to be more successful with the time-dependent conductivity than with the electron capture rate. The compensation of these phenomena could explain the temperature dependency on the observed conductivity decay rate.

3.2 Surface microscopy

Figure 4 shows a SEM image of a heterostructure GaAs/SnO_2:2%Eu (Fig. 4a) where some prominences are observed, which means most external particles. This sort of external particles is not found for SnO_2 samples where there is no GaAs bottom layer [12]. Such protuberances have a differential distribution of Eu^{3+} ions, which are more concentrated in these regions [12]. EDX general field of the same heterostructure shows the Sn and Eu distribution (Fig. 4b, c). It can be seen that there are regions where the Eu is more concentrated. These regions have been associated with the existence of Eu^{3+} PL bands in the GaAs/SnO_2 heterostructure, unlike SnO_2 films alone, which does not show emissions related to Eu^{3+} transitions [10, 12]. These Eu^{3+}-rich concentration protuberances may also contribute for the electrical transport in the GaAs/SnO_2 heterostructure, since Eu^{3+} acts as acceptor in the SnO_2 matrix and the electrical trapping in these areas may lead to different decay behavior, considering

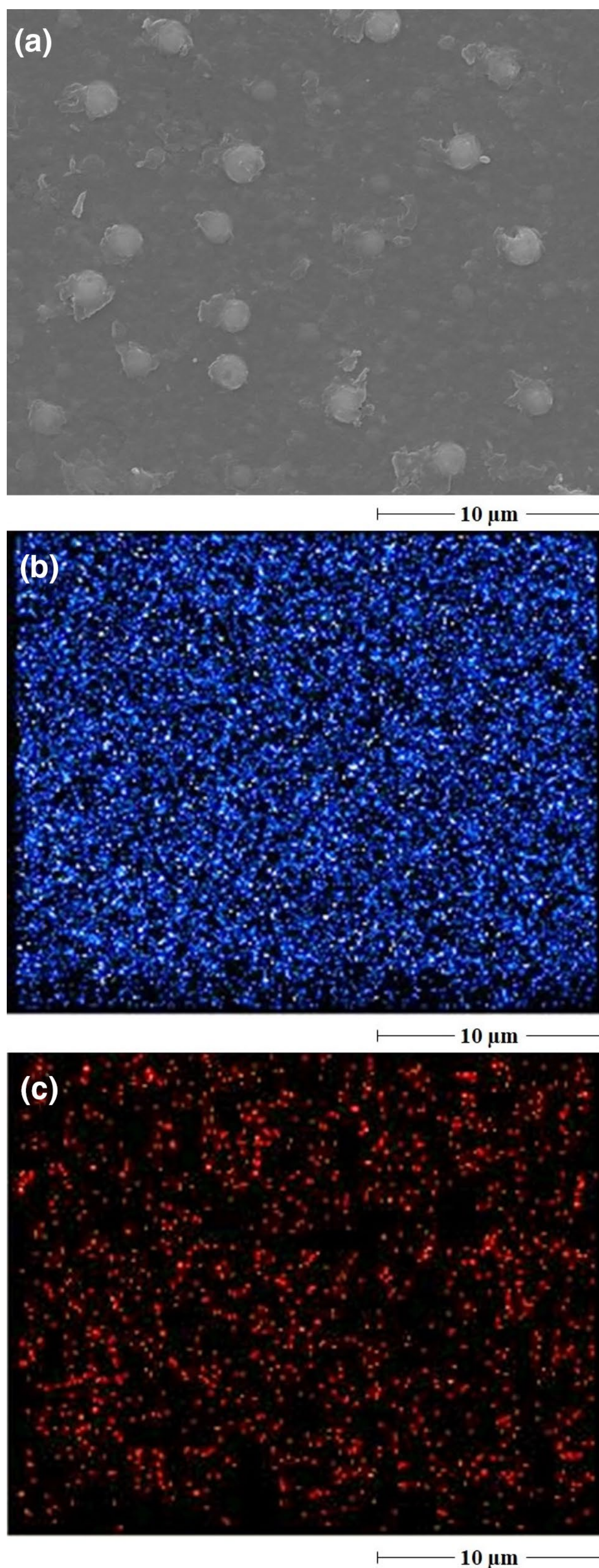

Fig. 4 SEM (magnitude ×10,000) of the heterostructure GaAs/SnO_2:2%Eu: **a** thermally annealed at 400 °C. **b, c** EDX general field of the same heterostructure, showing the Sn and Eu distribution, respectively

Table 2 Percentage of excitation from initial value of current in the dark compared to the maximum excited value for heterostructure GaAs/SnO_2:2%Eu

GaAs/SnO_2:2%Eu	% of excitation from dark value, after illumination during 9 min	
Temperature (K)	LED InGaN ($\lambda = 450$ nm)	Laser He–Cd ($\lambda = 325$ nm)
50	616.7	246.4
75	402.9	–
100	170.6	168.8
150	121.7	125.5
190	103.4	105.6
200	101.8	106.5

Table 3 Percentage of decay heterostructure GaAs/SnO_2:2%Eu from initial value at 600 s after excitation

GaAs/SnO2:2%Eu	% Decay at 600 s. Excitation with:	
Temperature (K)	LED InGaN ($\lambda = 450$ nm)	Laser He–Cd ($\lambda = 325$ nm)
50	78.8	56.0
75	69.2	–
100	39.8	38.9
150	17.0	19.3
190	3.1	2.2
200	1.6	3.1

the trapping by agglomerates and the low mobility in these regions.

3.3 Analysis of the temperature-dependent photo-induced current decay

Table 1 shows values of current for heterostructure GaAs/SnO_2:2%Eu for different excitation temperatures: current in the dark before monochromatic light excitation (I_{dark}), saturation current reached after 9 min of irradiation, current at 0 s of the decay data ($I_{initdecay}$) and current just after 10 min of decay [600 s in Fig. 2 (I_{after})]. The excitation to lower values for temperatures until 100 K in the case of the He–Cd laser means that the electrons excited to the GaAs side does not participate in the conduction process. Then, the LED excitation seems to be much more effective. On the other hand, when the temperature is raised the excitation with the laser becomes more effective, because the interface potential barrier is not high enough to avoid the thermally excited migration back of electrons, which, in this case, have enough thermal energy.

Table 2 shows the percentage of current excitation from its dark value before illumination (I_{dark}), compared to the maximum current at saturation, 9 min of excitation with

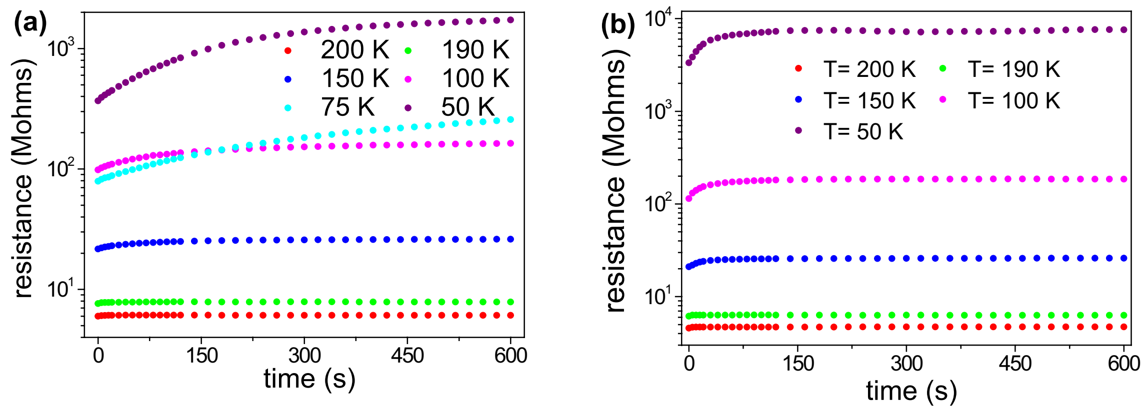

Fig. 5 Resistance as function of time for the heterostructure GaAs/SnO_2:2%Eu with annealing at 200°C/1 h, excited with two distinct light sources: **a** LED InGaN (450 nm) and **b** laser He–Cd (325 nm). The resistance data are obtained from the decay curve, after irradiation is removed

each light source ($I_{initdecay}$), which are evaluated using the experimental values given in Table 1.

Using again data from Table 1, the percentage of current decay from initial value ($I_{initdecay}$) until final current value (I_{after}) was evaluated, and it is shown in Table 3, which evidences that until about 100 K, the LED excitation leads to faster decay when compared to laser excitation, which does not hold for temperatures above 100 K. This is also consistent with electron trapping at interface GaAs/SnO_2 which only participates in the conduction process when the electrons have energy enough to overcome the interface barrier.

Looking at data from Tables 1 and 2, it is noticed that there is a higher excitation in the current as the temperature is decreased. In temperatures close to the room temperature, the He–Cd laser illumination is more effective in the current, which does not hold for lower temperatures where the InGaN LED excites much more the sample. It may be concluded that there are two regimes of excitation depending on temperature: below 100 K, where the LED excitation leads to a significantly higher increase in the current, whereas above 100 K laser excitation leads to a slightly higher value. The same tendency is observed for the decay, as seen in Table 3: the heterostructure GaAs/SnO_2:2%Eu shows higher percentage of decay (faster decay) for LED excitation, at lower temperatures, and this tendency is changed for higher temperatures, where, in general, the decay percentage at 600 s is higher for the He–Cd laser excitation.

As pointed out in Sect. 2, these decay data may be used for evaluation of $(E_{cap}-\phi)$. Then, plotting resistance as function of time, obtained from the decay data, using both excitation sources, InGaN LED and He–Cd laser, yield the curves shown in Fig. 5.

Figure 5 makes clear that the time dependence of resistance is not linear for the whole measured time (600 s), as would be expected for Eq. (1). This is related to distinct trapping centers, which have distinct capture cross-section, and distinct intrabandgap energy levels. Then the plot of $\ln(tgR/T) \times T^{-1}$ for different time intervals was used, where the curve can be considered as approximately linear for all the measured temperatures. Figure 6 shows used intervals and the respective plot of $\ln(tgR/T) \times T^{-1}$ for decay data from InGaN LED excitation.

The same procedure was carried out for current decay data of the heterostructure GaAs/SnO_2:2%Eu with laser He–Cd excitation (325 nm). These results are presented in Fig. 7. Table 4 brings the main features obtained from the results shown in Figs. 6 and 7, as the capture energy for the evaluated time ranges.

Curves shown in Figs. 6 and 7 exhibit positive inclination, which means that $(E_{cap}-\phi)$ presents a similar behavior to the case of Sb-doped SnO_2 [34], unlike the case of Er- or Eu-doped SnO_2 [29, 33]. One must recall that the main difference here is that the SnO_2 layer is deposited on top of a GaAs layer in the heterostructure assembly. The main electrical transport takes place in the top SnO_2 layer which is clearly observed in Table 1, by the low current values, even after intense photoexcitation, which is usual for rare-earth-doped SnO_2, where there is large charge compensation. Although the possibility of interface conduction by a 2DEG-like channel has been found in this sort of heterostructure [18], the values observed here assures that this sort of phenomena is not happening here, after photoexcitation of carriers to the interfacial layer. Then the main difference concerning the interface is the possibility that excited electrons may overcome the interface barrier as shown in Fig. 3, leading to distinct interpretations for the cases of InGaN LED or He–Cd laser excitation. However, considering that the main transport is taking place in the SnO_2 layer, it may assumed that ϕ and E_{cap} parameters, obtained from the modeling of photo-induced current decay, belong to the Eu-doped SnO_2

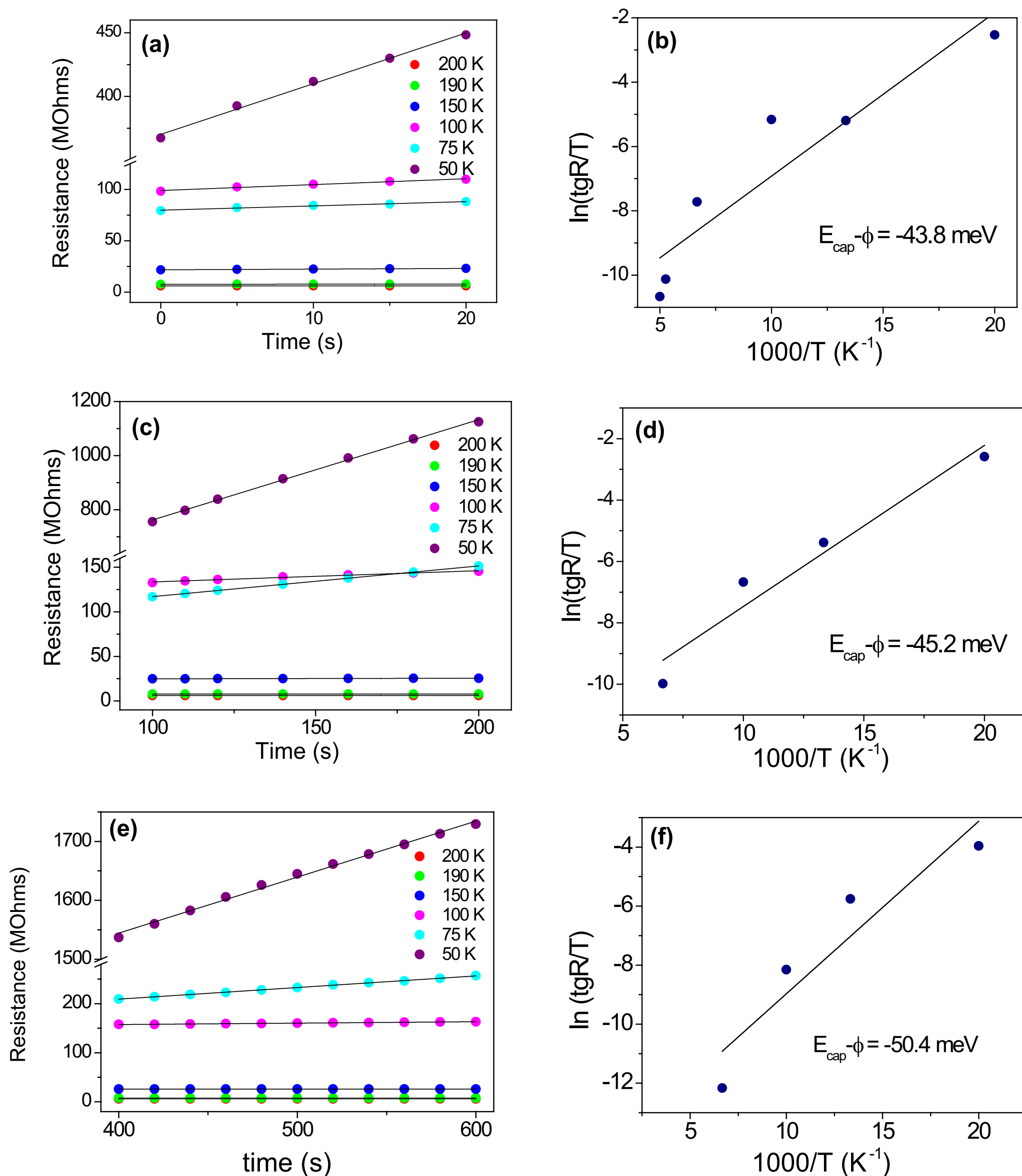

Fig. 6 Resistance as function of time: **a** 0–20 s, **c** 100–200 s and **e** 400–600 s (left), and corresponding plots of $\ln(tgR/T) \times T^{-1}$, **b, d** and **f** for excitation with InGaN LED (right)

matrix. Although the grain boundary barrier height is a function of temperature, using the average value of 0.7 eV for ϕ [34], we may estimate the E_{cap} value, which is 656 meV (0–20 s), 655 meV (100–200 s) and 650 meV (400–600 s) for excitation with the LED, and 640 meV (0–20 s) and 620 meV (400–600 s) for excitation with the laser. Comparing the same time range in both cases (0–20 and 400–600 s), it is observed that E_{cap} is lower than the grain boundary potential energy (0.7 eV), justifying the positive inclination in the plot of $\ln(tgR/T) \times T^{-1}$. For the case of He–Cd laser excitation, there are many oscillations in the curves of resistance as function of time, which are masked in Fig. 5 by the log nature and by the large scale of the y-axis and, then, an E_{cap} value for the range 20–400 s was not possible to be obtained. Looking again at Fig. 2, it is noticed that these oscillations for excitation with the laser are present in the decay curve as well, unlike the decay for the excitation with the LED (Fig. 2a), justifying the difficulties in obtaining

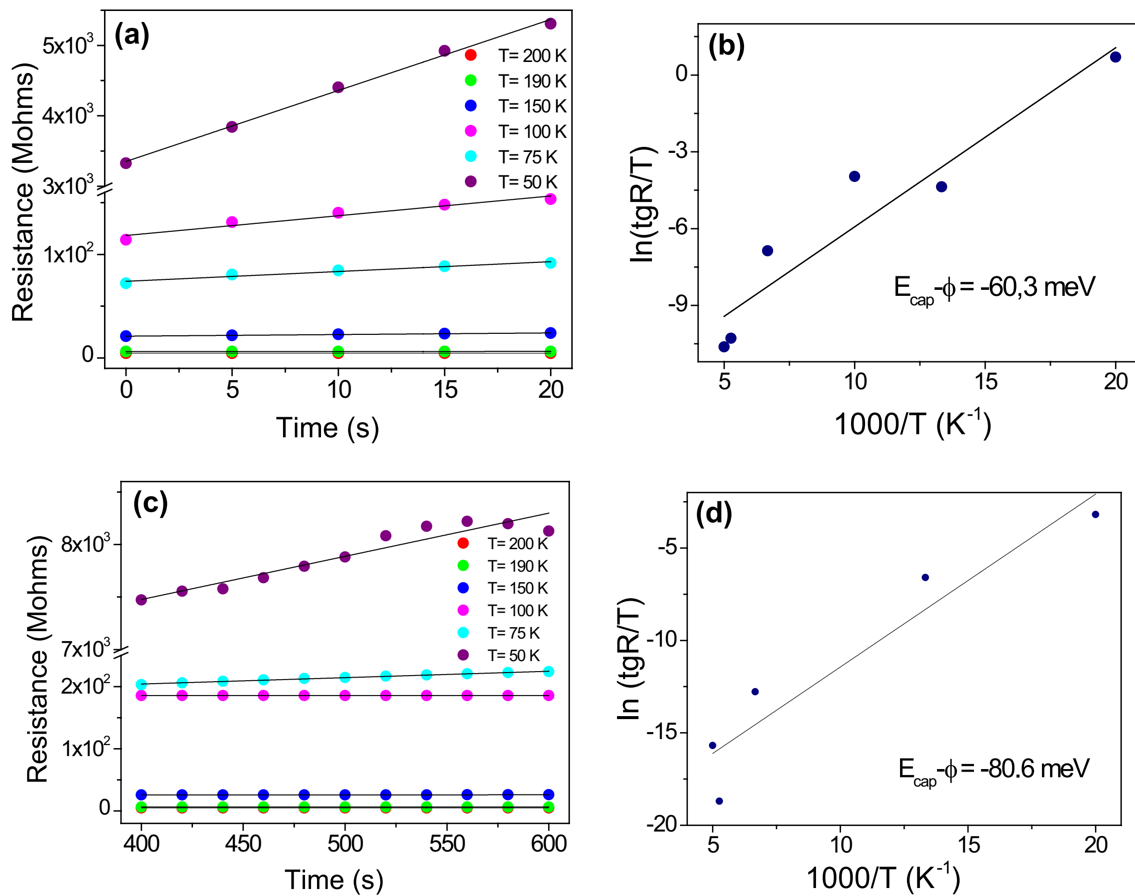

Fig. 7 Resistance as function of time: **a** 0–20 s and **c** 400–600 s (left), and respective plots of ln(tgR/T) × T^{-1} (**b, d**) (right). Excitation with the He–Cd laser

Table 4 Evaluation of E_{cap}–ϕ, results obtained from Figs. 4 and 5

Excitation source	E_{cap}–ϕ (meV)	E_{cap} (meV) (*)
LED InGaN (450 nm)	– 43.8 (0–20 s)	656.2
	– 45.2 (100–200 s)	654.8
	– 50.4 (400–600 s)	649.6
Laser He-Cd (325 nm)	– 60.3 (0–20 s)	639.7
	– 80.6 (400–600 s)	619.4

(*) (considering ϕ = 0.7 eV [35])

an E_{cap} value for intermediate time. Considering the different values for different time ranges, it seems reasonable to assume that a distribution of defects with three distinct capture energies is expected, mainly taken into account the highly disordered structure of the sol–gel film, deposited on top of GaAs in the heterostructure. The impossibility of obtaining an E_{cap} value for the laser excitation in the range

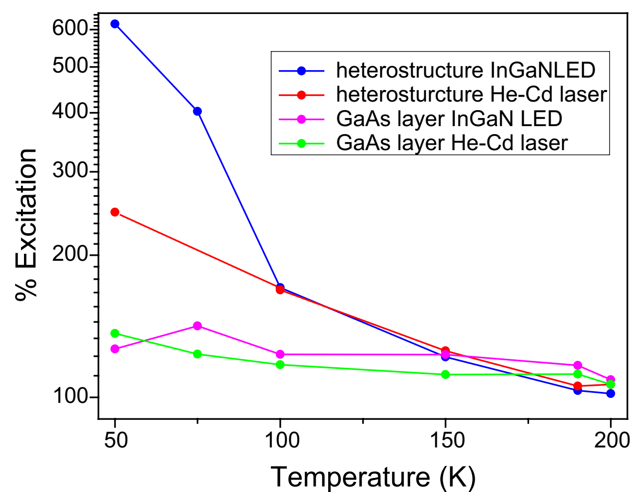

Fig. 8 Current excitation percentage for heterostructure GaAs/SnO_2:2%Eu and GaAs thin film for distinct temperatures and light sources. Data are obtained at fixed temperatures. Lines are drawn just as a guide for the eyes

20–400 s reinforces this hypothesis. Then, there are at least three main defects: oxygen vacancies, Eu^{3+} acceptors and agglomerates of Eu^{3+} acceptors as identified with SEM procedures (Fig. 4). It is important to mention that the capture energy is not exclusively related with the energy level in the bandgap, but with the lattice relaxation involved in the trapping process. Besides, oxygen vacancies may surround the Eu^{3+} centers located at grain boundary [30], giving origin to distinct trapping kinetics, where the grain boundary energy and depletion layer become very important parts, as already discussed. Moreover, in the particular case of the laser excitation, the effective trapping by the defects must be corrected by the trapping at the interface barrier as suggested by the configurational diagram plotted in Fig. 3.

Recalling again that the trapping characteristics are mainly related to the SnO_2 top layer, the higher energy for the capture barrier after illumination may be associated to the generation of a metastable state with high electronic density in the conduction band. The illumination raises the Fermi level, which is already above the bottom of the conduction band [34]. Considering that laser allows electron–hole generation and intrabandgap states excitation, the position of the Fermi level for the laser-excited sample is higher than the sample excited with LED. As a consequence, the effective barrier seen by metastable excited electrons is less in the case of laser illumination [34]. Besides, particularly in the case of GaAs/SnO_2 heterostructure, presented in this paper, the slower current decay for the He–Cd laser-excited sample suggests that electrons may overcome the potential barrier at the heterostructure interface, as shown in Fig. 3, becoming located at the GaAs side, with slower return to the equilibrium state.

To visualize the excitation percentage in the current of the heterostructure GaAs/SnO_2:2%Eu using the two light sources, LED InGaN (450 nm) and laser He–Cd (325 nm), these data are plotted in Fig. 8. The degree of influence of the heterostructure assembly in this excitation behavior can also be verified when the same sort of data, a complete decay series for both monochromatic light excitations, are also registered for a sole GaAs film sample, quite similar to the layer deposited as bottom layer of the heterostructure. Then, all data concerning excitation percentage are also shown in Fig. 8.

Figure 8 clearly illustrates that for lower temperatures the excitation is more efficient in the heterostructure compared to the GaAs thin film alone. As the temperature is raised the excitation for both sort of samples gets closer. It must be recalled that all the excitation in the heterostructure samples are expected to be done mainly in the SnO_2 layer. The lower excitation in the GaAs sample means that either the He–Cd laser as well as the InGaN LED are more efficient excitation tools for the SnO_2 material, deposited on top of the heterostructure, than for GaAs, mainly at lower temperatures, considering that the laser is an ultraviolet source (3.82 eV) and the LED is a blue source (2.76 eV), and both are way above the bandgap of GaAs (about 1.42 eV for single-crystal sample). Anyway the decay in GaAs (not shown in this paper) does not follow any tendency, which could be associated with the amorphous structure of the resistively evaporated GaAs material, and the highly disordered configuration, with no preferential trapping by existing defects. Surprisingly, the relative excitation is of the same order of magnitude of the excitation in the heterostructure sample, mainly above 100 K, meaning that although the excitation energy is rather higher than the bandgap energy of the GaAs single crystal, in this sort of material, resistively evaporated, ionizing centers may be present, which is a matter for future research.

4 Conclusion

The photo-induced decay in the GaAs/SnO_2 heterostructure samples leads to a behavior similar to what was observed previously to Sb-doped SnO_2 and unlike Eu-doped SnO_2 films deposited on glass substrates. Considering that the electrical transport is mainly determined by the top layer in the heterostructure, the differences compared to the previously observed Eu-doped samples are mainly related to the film interface, which allows electron arrest, leading to slower decay mainly below 100 K. Although electrons are excited to overcome the interface barrier, a 2DEG-like behavior was not observed, since the conductivity is quite low and the SnO_2 top layer dominates the transport properties.

The assembly of a GaAs/SnO_2 heterostructure, where the top oxide layer is doped with Eu^{3+}, have the electrical transport properties also influenced by the existence of Eu^{3+}-agglomerates in the SnO_2 surface, because the trapping in these agglomerates may lead to different decay behavior, considering the trapping by closely located defects and the low mobility in these regions.

The modeling of the photo-induced decay data helps understanding the electrical properties of this sort of heterostructure which, allied to the emission properties, leads to the potential design of optoelectronic devices.

Acknowledgements Authors thank the Brazilian financial Agencies CNPq (Grant 305963/2016-3) and CAPES. Authors also thank Prof. Margarida J. Saeki for the MEV-EDX data.

References

1. E. Monroy, F. Omnés, F. Calle, Semicond. Sci. Technol. **18**, R33–R51 (2003)
2. H. Hosono, Thin Solid Films **515**, 6000–6014 (2007)

3. T. Li, W. Zeng, H. Long, Z. Wang, Sens. Actuators B Chem **231**, 120–128 (2016)
4. E. Dien, J.M. Laurent, A. Smith, J. Eur. Ceram. Soc. **19**, 787–789 (1999)
5. V. Geraldo, L.V.A. Scalvi, P.N. Lisboa-Filho, C. Morilla-Santos, J. Phys. Chem. Solids **67**, 1410–1415 (2006)
6. K. Bouras, G. Schmerber, H. Rinnert, H.D. Aureau, H. Park, G. Ferblantier, S. Colis, S.T. Fix, C. Park, W.K. Kim, A. Dinia, A. Slaoui, Sol. Energy Mat. Sol. Cells **145**, 134–141 (2016)
7. T. Asar, B. Korkmaz, S. Özçelik, J. Exp. Nanosci. **11**, 1285–1306 (2016)
8. S. Gürakar, T. Serin, N. Serin, Adv. Mat. Lett. **5**, 309–314 (2014)
9. M. Ishii, S. Komuro, T. Morikawa, J. Appl. Phys. **94**, 3823–3827 (2013)
10. E.A. Morais, L.V.A. Scalvi, A. Tabata, J.B.B. Oliveira, S.J.L. Ribeiro, J. Mater. Sci. **43**, 345–349 (2008)
11. E.A. Morais, L.V.A. Scalvi, S.J.L. Ribeiro, V. Geraldo, Phys. Status Solidi (a) **202**, 301–308 (2005)
12. C.F. Bueno, L.V.A. Scalvi, M.S. Li, M.J. Saeki, Opt. Mater. Express **5**, 59–72 (2015)
13. S. Adachi, J. Appl. Phys. **58**, R1 (1985)
14. E. Cuculescu, I. Evtodiev, M. Caraman, Thin Solid Films **517**, 2515–2518 (2009)
15. Y. Liu, Y.Jiao,Z. Zhang, F. Qu, A. Umar, X. Wu, ACS Appl. Mater. Interfaces **6**, 2174–2184 (2014)
16. G.-H. X.Cui, Y.D. Lee, P.Y. Kim, Arefe,, C.-H. Huang, D.A. Lee, X. Chenet, L. Zhang, F. Wang, Ye,.B.S. Pizzocchero, K. Jessen, T. Watanabe, D.A. Taniguchi, T. Muller, P. Low, J. Kim, Hone, Nat. Nanotechnol. **10**, 534–540 (2015)
17. P. Gehring, R. Urcuyo, D.L. Duong, M. Burghard, K. Kern, Appl. Phys. Lett. **106**, 233110(1–5) (2015)
18. T.F. Pineiz, L.V.A. Scalvi, M.J. Saeki, E.A. Morais, J. Electron. Mater. **39**, 1170–1176 (2010)
19. T.F. Pineiz, E.A. Morais, L.V.A. Scalvi, C.F. Bueno, Appl. Surf. Sci. **267**, 200–205 (2013)
20. C.F. Bueno, L.V.A. Scalvi, Thin Solid Films **612**, 303–309 (2016)
21. D.H.O. Machado, L.V.A. Scalvi, A. Tabata, J.H.D. da Silva, J. Mater. Sci. Mater. Electron. **28**, 5415–5424 (2017)
22. D.J. Chadi, K.J. Chang, Phys. Rev. B **39**, 10063–10074 (1989)
23. E.A. Morais, L.V.A. Scalvi, V. Geraldo, R.M.F. Scalvi, S.J.L. Ribeiro, C.V. Santilli, S.H. Pulcinelli, J. Eur. Ceram. Soc. **24**, 1857–1860 (2004)
24. E.R. Viana, J.C. Gonzalez, G.M. Ribeiro, A.G. Oliveira, J. Phys. Chem. C **117**, 7844–7849 (2013)
25. S. Chitra, D. Easwaramoorthy, S.N. Jayanthi, S. Shanthi, Int. J. Chem. Tech. Res. **6**, 4722–4728 (2014)
26. E.A. Morais, L.V.A. Scalvi, J. Mater. Sci. **42**, 2216–2221 (2007)
27. P.M. Mooney, G.A. Northrop, T.N. Morgan, H.G. Grimmeiss, Phys. Rev.B **37**, 8298–8307 (1988)
28. T.W. Dobson, L.V.A. Scalvi, J.F. Wager, J. Appl. Phys. **68**, 601–605 (1990)
29. E.A. Morais, L.V.A. Scalvi, J. Eur. Ceram. Soc. **27**, 3803–3806 (2007)
30. V. Geraldo, V. Briois, L.V.A. Scalvi, C.V. Santilli, J. Eur. Ceram. Soc. **27**, 4265–4268 (2007)
31. E. Boyalı, V. Baran, T. Asar, S. Ozçelik, M. Kasap, J Alloys Compd. **692**, 119–123 (2017)
32. D.H. Zhang, H.L. Ma, Appl. Phys. A **62**, 487–492 (1996)
33. E.A. Morais, L.V.A. Scalvi, A.A. Cavalheiro, A. Tabata, J.B.B. Oliveira, J. Non-Cryst. Solids **354**, 4840–4845 (2008)
34. E.A. Floriano, L.V.A. Scalvi, J.R. Sambrano, A. de Andrade, Appl. Surf. Sci. **267**, 164–168 (2013)
35. M.A.L. Pinheiro, T.J. Pineiz, E.A. Morais, L.V.A. Scalvi, M.J. Saeki, A.A. Cavalheiro, Thin Solid Films **517**, 976–981 (2008)